# Numerical Simulation of the Transonic Flowfield for Wing/Nacelle Configurations

Essam H. Atta* and Joseph Vadyak*
*Lockheed-Georgia Company, Marietta, Georgia*

**An efficient grid-interfacing zonal algorithm has been developed for computing the three-dimensional transonic flowfield about wing/nacelle multicomponent configurations. The algorithm uses the full-potential formulation and the AF2 fully implicit approximate factorization scheme. The flowfield solution is computed using a component-adaptive grid approach in which separate grids are employed for the individual components in the multicomponent configuration, where each component grid is optimized for a particular geometry such as the wing or nacelle. The wing and nacelle component grids are allowed to overlap, and flowfield information is transmitted from one grid to another through the overlap region using trivariate interpolation. This paper presents a discussion of the computational methods used to generate both the wing and nacelle component grids, the technique used to interface the component grids, and the method used to obtain the inviscid multicomponent flowfield solution. Computed results and correlations with experiment are presented to illustrate application of the analysis.**

## Introduction

RELIABLE and efficient three-dimensional transonic flow analysis methods are required to make realistic and cost-effective predictions of aircraft aerodynamics. Early efforts to predict the transonic flowfield about aircraft multicomponent configurations are based on the transonic small-disturbance formulation.[1] This allows the geometry of the configuration to be greatly simplified and the surface boundary conditions to be applied on a mean approximate surface. Accurate prediction of such flowfields, however, requires the use of the full-potential formulation and the generation of a suitable surface-fitted grid. Because each aircraft component (wing, nacelle, fuselage) requires, in general, a grid system that is usually incompatible with the grid systems of the other components, the generation of a single surface-fitted grid for the entire configuration is a difficult task. In such a global grid, control of grid-point distribution, skewness, and clustering would be difficult to achieve. However, the single grid approach was used in Ref. 2 and produced reasonable results.

In the present investigation,[3] an alternate approach is employed. The approach taken is to use a component-adaptive grid-embedding scheme in which the global computational grid is composed of a series of overlapped component grids. The AF2 approximate factorization algorithm[4,5] is used to determine the conservative full-potential equation solution on each component grid with trivariate interpolation used to transfer property information between the component grids.

Using the component-adaptive grid approach requires that the grid-generation and flow solution algorithms be available for each component in the configuration. In the present investigation, the NASA Ames GRGEN3 wing grid-generation program and the TWING transonic wing flow analysis program[5,6] are employed in computing the wing component flowfield. To determine the nacelle component flowfield, the NGRIDA nacelle grid-generation program and the NACELLE nacelle flow analysis program are employed.[7] The TWING and NACELLE programs have been combined to produce a wing/nacelle multicomponent flow analysis algorithm called TWN.[8]

Received Nov. 28, 1984; revision received Aug. 9, 1985. 

*Scientist, Advanced Flight Sciences Department. Member AIAA.

## Component Grid Topology and Generation

The global computational grid is composed of the wing and nacelle component grids, each of which is generated separately. Each component grid is body-fitted and computed using a numerical grid-generation algorithm.

### Wing Component Grid Generation

The wing flowfield solution is computed on a three-dimensional body-fitted curvilinear mesh. The wing computational mesh is obtained using two-dimensional numerical grid-generation techniques for a series of spanwise stations distributed along the wingspan starting at the root symmetry plane and progressing past the wingtip into the far field.

Figure 1 illustrates the O-type body-fitted grid for an isolated wing. The base Cartesian coordinates are denoted by $x$, $y$, and $z$. The computational curvilinear coordinates are denoted by $\xi$, $\eta$, and $\zeta$.

The wing surface grid points are clustered near the wing leading and trailing edges using either a conformal mapping distribution or a geometric stretching function expressed in terms of the arc length measured from the wing edge points. The outer boundary points are distributed at equal angular increments around the body.

Once the wing surface and outer boundary mesh-point distributions have been determined for a given spanwise station, the interior mesh-point locations are determined by iteratively solving the two coupled Laplace equations:

$$\xi_{xx} + \xi_{zz} = 0 \tag{1}$$

$$\zeta_{xx} + \zeta_{zz} = 0 \tag{2}$$

These equations are transformed into and solved in the computational domain. An alternating-direction-implicit (ADI) relaxation algorithm is used to solve the governing finite difference equations.[6] This then establishes the grid-point coordinates at each spanwise station used in defining the wing geometry. Clustering of the spanwise stations is performed in the vicinity of the wing root, wingtip, and wingspan locations of the nacelle.

Figure 1 shows the isolated wing grid topology. To use the isolated wing grid in the present multicomponent flowfield analysis, selected interior mesh points are deleted from the

grid to accommodate the nacelle geometry. Figure 2 illustrates a view of the wing grid at a span station that contains the nacelle. The aperture in the interior of the grid in physical space creates an irregularly shaped void in the wing computational space domain.

### Nacelle Component Grid Generation

The nacelle flowfield solution is computed on a three-dimensional body-fitted curvilinear computational mesh. The nacelle computational mesh is obtained by using two-dimensional, numerical, grid-generation techniques for a series of meridional planes placed circumferentially around the body (a meridional plane contains the longitudinal axis of the inlet).

Figure 3 illustrates the C-type nacelle/inlet body-fitted grid for a nacelle extended in the downstream direction. Figure 3 shows the meridional plane grid topology. If a pylon were present, the pylon geometry would be contained between two meridional stations. However, this option has not been implemented in the current version of the code.

The surface grid points are clustered in the region of the nacelle hilite (leading-edge point of the nacelle). The clustering is achieved by using a geometric stretching function expressed in terms of the arc length measured along the body from the hilite point. The outer computational boundary point distribution is determined by using either an angular distribution function expressed in terms of an angle measured about the nacelle hilite, or by using an arc length distribution along the outer boundary.

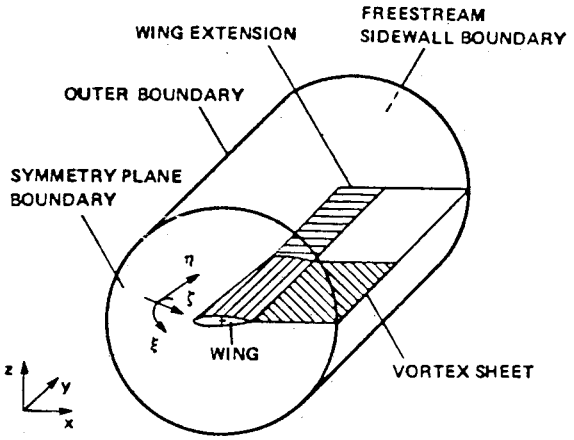


Fig. 1 Isolated wing grid topology.

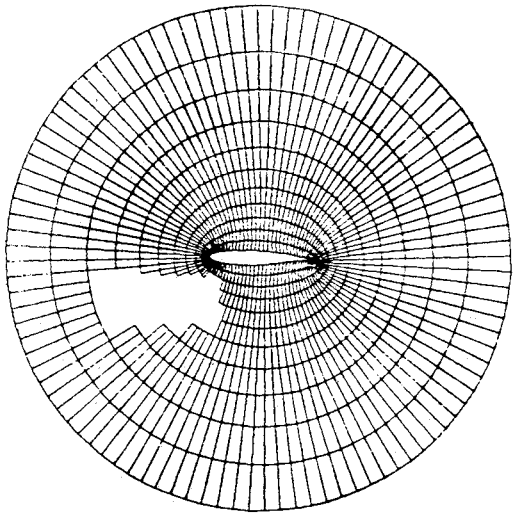

Fig. 2 Side view of wing component grid at a span station containing the nacelle.

Once the surface and outer boundary mesh-point distributions have been determined, the interior mesh-point locations are computed using the NASA Ames GRAPE[9] algorithm. The GRAPE algorithm determines the interior field point coordinates by iteratively solving two-coupled Poisson equations. For axisymmetric geometries, this two-dimensional grid-generation procedure is applied for only one meridional plane, and the grid-point locations on the remaining meridional planes are found by using simple reflection techniques. For asymmetric geometries, the two-dimensional grid-generation algorithm can be applied for each meridional plane.

Figure 4 illustrates a typical meridional plane interface grid. The inlet centerline—the $x$ axis—represents a singularity in the three-dimensional grid mapping. The computational grid boundary is displaced a small distance away from the $x$ axis. An extrapolation and averaging technique, described later, is used to obtain flow properties on the centerline.

## Governing Equations for the Inviscid Flow

The inviscid flow gas dynamic model is based on the assumption of steady potential flow which requires that the flow be both irrotational and isentropic. The governing equations for steady three-dimensional potential flow are given by

$$\left(\frac{\rho U}{J}\right)_{\xi}+\left(\frac{\rho V}{J}\right)_{\eta}+\left(\frac{\rho W}{J}\right)_{\zeta}=0 \tag{3}$$

$$\rho=\left[1-\frac{\gamma-1}{\gamma+1}\left(U\phi_{\xi}+V\phi_{\eta}+W\phi_{\zeta}\right)\right]^{\frac{1}{\gamma-1}} \tag{4}$$

where $\xi$, $\eta$, and $\zeta$ denote the system of curvilinear coordinates; $U$, $V$, and $W$ are the contravariant velocity components in the $\xi$, $\eta$, and $\zeta$ directions, respectively; $\rho$ the density; $J$ the Jacobian of transformation from the Cartesian coordinate system $(x,y,z)$ to the general curvilinear coordinate system $(\xi, \eta, \zeta)$; $\phi$ the velocity potential function; and $\gamma$ the specific heat ratio. The density and contravariant velocity components are normalized by the stagnation density and critical sonic speed, respectively.

Equation (3) is the full-potential equation in strong conservation law form. It expresses mass continuity for steady three-dimensional flows. Equation (4) expresses entropy conservation and is used to compute the density given the velocity potential field.

## Numerical Algorithm

### Basic Finite-Difference Scheme

The present numerical algorithm is based on the finite difference formulation used by Holst and Thomas[6] in computing transonic wing flows. In this algorithm, the full-potential

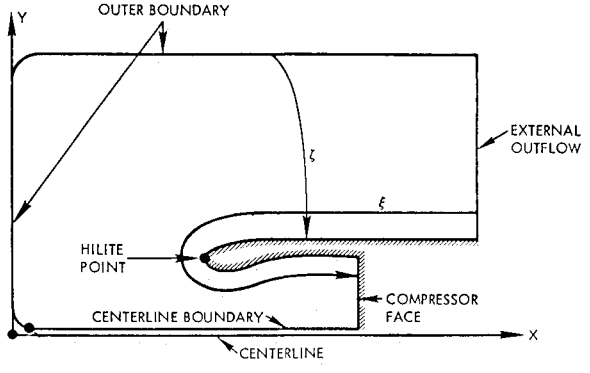


Fig. 3 Isolated nacelle grid topology.

equation residual is given by

$$L\phi_{i,j,k} = \bar{\delta}_{\circ}{}'_{\xi}\left(\frac{\tilde{\rho}U}{J}\right)_{i+\frac{1}{2},j,k} + \bar{\delta}_{\circ}{}'_{\eta}\left(\frac{\tilde{\rho}V}{J}\right)_{i,j+\frac{1}{2},k} + \bar{\delta}_{\zeta}\left(\frac{\hat{\rho}W}{J}\right)_{i,j,k+\frac{1}{2}} \tag{5}$$

where $L\phi_{i,j,k}$ denotes the residual operator, and $i$, $j$, and $k$ denote the grid-point indices in the $\xi$ (wraparound), $\eta$ (circumferential or spanwise), and $\zeta$ (radial) directions, respectively. The operators $\bar{\delta}_{\xi}(\,)$, $\bar{\delta}_{\eta}(\,)$, and $\bar{\delta}_{\zeta}(\,)$, are first-order accurate backward finite difference operators (applied at midpoints) for the $\xi$, $\eta$, and $\zeta$ directions, respectively. The terms $\tilde{\rho}$, $\tilde{\rho}$, $\hat{\rho}$ are upwind-biased density coefficients given by expressions of the form

$$\tilde{\rho}_{i+\frac{1}{2},j,k} = [(1-\upsilon)\rho]_{i+\frac{1}{2},j,k} + \upsilon_{i+\frac{1}{2},j,k}\ \rho_{i+\frac{1}{2}+r,j,k} \tag{6}$$

where $r$ denotes an upwind point along the $\xi$ direction, and $\upsilon$ an artificial viscosity coefficient. In Eq. (6), the physical density $\rho$ is computed using Eq. (4) with central differences used to determine the derivatives of $\phi$. The artificial viscosity coefficient $\upsilon$ is given by

$$\begin{aligned} \upsilon &= 0 && \text{if } M_{i,j,k} < 1 \\ &= C(M^2_{i,j,k} - 1) && \text{if } M_{i,j,k} > 1 \end{aligned} \tag{7}$$

where $M$ is the local Mach number, and $C$ a user-specified constant. The artificial viscosity coefficient $C$ typically ranges from 1.0 to 2.0, with the larger values producing greater upwinding. Expressions similar to Eq. (7) hold for $\tilde{\rho}$ and $\hat{\rho}$ which affect upwinding in the $\eta$ and $\zeta$ directions, respectively.

The finite difference equations are solved using the efficient AF2 approximate factorization scheme.[6] The AF2 algorithm is written in a three-step form as

$$\left(\alpha - \frac{1}{A_k}\bar{\delta}_{\eta}\, A_j \bar{\delta}_{\eta}\right) g^n_{i,j} = \alpha\omega L\phi^n_{i,j,k} + A_{k+1} f^n_{i,j,k+1} \tag{8}$$

$$\left(A_k \mp \beta_{\xi}\bar{\delta}_{\xi} - \frac{1}{\alpha}\bar{\delta}_{\xi} A_i \bar{\delta}_{\xi}\right) f^n_{i,j,k} = g^n_{i,j} \tag{9}$$

$$(\alpha + \bar{\delta}_{\zeta}) C^n_{i,j,k} = f^n_{i,j,k} \tag{10}$$

In Eqs. (8-10), $\alpha$ is a time-like factorization parameter chosen to maintain stability and attain fast convergence, $\beta_{\xi}$ a factor that controls the amount of dissipation required in regions of supersonic flow, $\omega$ a relaxation factor, $n$ the iteration number, $L\phi_{i,j,k}$ the mass residual [defined by Eq. (5)], $f$ and $g$ intermediate functions obtained during the solution process, and $C_{i,j,k}$ the potential function correction given by

$$C^n_{i,j,k} = \phi_{i,j,k}{}^{n+1} - \phi^n_{i,j,k} \tag{11}$$

The terms $A_i$, $A_j$, and $A_k$ are defined by

$$A_i = (\tilde{\rho}A_1/J)^n_{i-\frac{1}{2},j,k} \tag{12}$$

$$A_j = (\tilde{\rho}A_2/J)^n_{i,j-\frac{1}{2},k} \tag{13}$$

$$A_k = (\hat{\rho}A_3/J)^n_{i,j,k-\frac{1}{2}} \tag{14}$$

In the first two steps functions $g$ and $f$ are obtained by solving a tridiagonal system of equations, while in the third step the correction $C_{i,j,k}$ is obtained by solving a bidiagonal system of equations.

The iterative relaxation procedure can be viewed as a time-marching integration algorithm in pseudotime. Using this analogy, the factorization parameter $\alpha$ appearing in Eqs. (8-10) can be regarded as the reciprocal of the marching pseudotime step. To eliminate all components of the error frequency spectrum, it is generally preferable to employ a variable time step which sequentially varies with iteration number.

The factorization parameter $\alpha$ is computed using a repeating sequence based on iteration number.[4] The $\alpha$ sequence employed is given by

$$\alpha_k = \alpha_h (\alpha_1/\alpha_h)^{(k-1)/(M-1)} \qquad (k = 1,2,\cdots,M) \tag{15}$$

where $\alpha_l$ is the lower limit of $\alpha$, $\alpha_h$ the upper limit, and $\alpha_k$ the value of $\alpha$ for the $k$th element of the sequence. For all of the cases presented herein, the number of elements in the sequence $M$ was equal to 8. The optimum values of $\alpha_l$ and $\alpha_h$ are generally determined by numerical experiment.

**Boundary Conditions**

At the surface of the wing or nacelle, the contravariant velocity $W$ in the $\zeta$-coordinate direction is equated to zero as this satisfies the flow tangency condition.

At the compressor face outflow surface inside the inlet, the contravariant velocity $U$ in the $\xi$-coordinate direction is specified. Given the local Cartesian velocity components $u,v$, and $w$, and the metric quantities $\xi_x, \xi_y$, and $\xi_z$, $U$ can be determined. At the compressor face, the flow is assumed to be uniform and in the axial ($x$) direction. The local flow velocity and density are fixed by specification of the required engine mass flow rate.

For the nacelle component algorithm, the grid centerline boundary is offset a small distance from the centerline to avoid the mapping singularity at the centerline. To determine property values on the centerline, an extrapolation and averaging procedure is employed, which is fully discussed in Ref. 7.

At the wing symmetry plane boundary, the contravariant velocity $V$ in the $\eta$-coordinate direction is equated to zero. At the wing freestream sidewall boundary, the initial freestream distribution of $\phi$ is held fixed as is the distribution for the wing grid outer boundary for nonlifting cases. For lifting calculations, the distribution on the wing grid outer boundary is updated using a compressible vortex solution.[6] The wing circulation is computed at the end of each wing algorithm iteration by calculating the potential jump along the vortex sheet.

The nacelle component grid outer boundary constitutes the grid overlap region outer boundary. The grid overlap region inner boundary is constituted by the irregularly shaped boundary obtained from deleting selected interior field points from the wing component grid in order to accommodate the nacelle geometry (see Fig. 2). For the overlap region inner and outer boundaries, the velocity potential $\phi$ or the velocity potential normal derivative $\phi_n$ can be specified. Both options were tried in two dimensions[10] and no significant differences in the final results were observed. However, specifying the velocity potential (which is a scalar quantity) is easier to implement and requires less computational effort as compared to specifying the velocity potential normal derivative.

The portion of the overlap region inner boundary adjacent to the engine exhaust plane at the aft end of the nacelle requires special treatment. A uniform axial velocity is specified at the nacelle aft station and a three-point extrapolated difference is used to provide the required values of the potential function at the wing grid points immediately downstream of this station.

In addition to specifying $\phi$ on the overlap region boundaries, it is necessary to specify boundary conditions for the $f$ and $g$ intermediate functions for use in the wing component algorithm. For the $f$ intermediate function in the $\xi$-wraparound coordinate direction, the Dirichlet boundary condition $f = 0$ is imposed on the overlap region inner boundary in performing the wing component flowfield calculations. For the $g$ intermediate function in the $\eta$-spanwise coordinate direction, the Neumann boundary condition $g_{\eta} = 0$ is imposed on

the overlap region inner boundary. Both the $f$ and $g$ values approach zero as the iterative procedure progresses and convergence is attained.

For the nacelle component algorithm, the Dirichlet boundary condition $f=0$ is imposed at the external outflow surface of the nacelle grid in solving the system of factorized difference equations in the $\xi$-wraparound coordinate direction. Periodic differencing is employed in the $\eta$-circumferential direction.

**Iteration Procedure**

The computation is started by initializing the entire velocity potential field. For the external flow around the wing and nacelle cowling, the initialization of the potential field is performed using freestream velocity components. For the internal flow initialization inside the inlet, the local velocity is assumed to be axial and is computed using a Mach number determined from the implicit relation

$$M\left(1+\frac{\gamma-1}{2}M^2\right)^{[-(\gamma+1)]/[2(\gamma-1)]}=\left(\frac{A_{cf}}{A}\right)M_{cf}\times\left(1+\frac{\gamma-1}{2}M_{cf}^2\right)^{[-(\gamma+1)]/[2(\gamma-1)]} \quad (16)$$

where $M$ and $M_{cf}$ denote the local and compressor face Mach numbers, respectively, and $A$ and $A_{cf}$ denote the local and compressor face flow areas, respectively. Equation (16) was obtained using one-dimensional gas dynamic formulas and simply expresses mass continuity for the captured stream tube. To determine the internal potential field, a trapezoidal rule integration is used. The compressor face Mach number $M_{cf}$ is fixed by specification of the required engine mass flow rate.

Once the entire potential field has been initialized, the wing algorithm is then executed for a specified number of iterations (typically 40 ~ 50) holding $\phi$ constant on the overlap inner boundary. The nacelle algorithm is then executed for a specified number of iterations (typically 40 ~ 50) using overlap outer boundary conditions as determined from the wing solution. At this stage, the wing algorithm is again executed using updated overlap inner boundary conditions obtained from the nacelle solution. This process is repeated until overall convergence is achieved. Typically 4-5 cycles are required for convergence with 40-50 iterations being performed in both the wing and nacelle component algorithms per cycle.

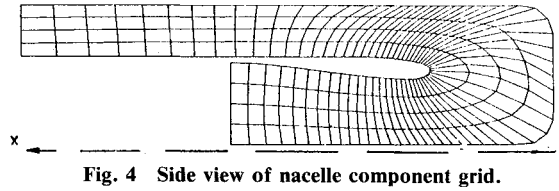

Fig. 4 Side view of nacelle component grid.

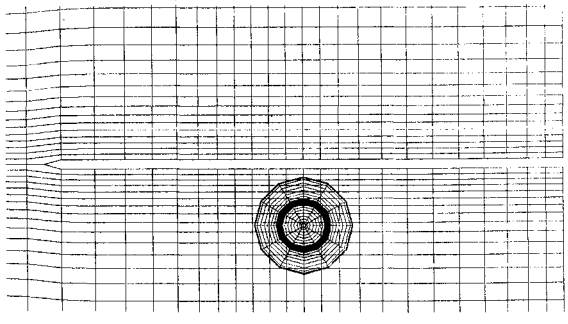

Fig. 5 Front view of NACA 0012-wing/GELAC1-nacelle configuration global grid.

**Intergrid Property Transfer**

Multivariate interpolation is employed to transfer property information between the component grids. To effect intergrid property transfer for the wing/nacelle configuration requires employing a trivariate interpolation polynomial since the component grids do not have a common coordinate surface. To reduce the coding logic, a trivariate polynomial based on a linear Taylor series expansion was employed. Interpolation is performed in computational $(\xi,\eta,\zeta)$ space using a polynomial of the form

$$f(\xi,\eta,\zeta)=f_0+f_{\xi_0}(\xi-\xi_0)+f_{\eta 0}(\eta-\eta_0)+f_{\zeta 0}(\zeta-\zeta_0) \quad (17)$$

where $f(\xi,\eta,\zeta)$ denotes the interpolated flow property at the point $(\xi,\eta,\zeta)$, and the subscript 0 denotes a selected interpolation base point in computational space.

The use of the trivariate interpolation polynomial given by Eq. (17) in some cases produced oscillations in the interpolated values of the velocity potential. The nacelle component grid lies in a region where the wing component grid is relatively coarse, thereby creating a disparity in the average cell size between the two grids in the overlap region where the interpolation is performed. It was found that the best results were obtained by employing a relatively fine grid for the wing and a relatively coarse grid for the nacelle. To ensure a monotonic behavior for the interpolated overlap boundary potential values, explicit cubic polynomial smoothing is performed on the velocity potential in the streamwise direction after each cycle of the wing/nacelle solution.

## Numerical Results

Selected numerical results are now presented to illustrate application of the analysis.

The first set of computed results is for a simplified wing/nacelle configuration. The wing geometry is represented by an NACA 0012 wing with an aspect ratio of 6.0, zero twist, and is unswept and untapered. The nacelle geometry is represented by the Lockheed-Georgia GELAC1 axisymmetric nacelle/inlet configuration.[7] The nacelle is located at the 50% span station and has its axis parallel to the wing chord.

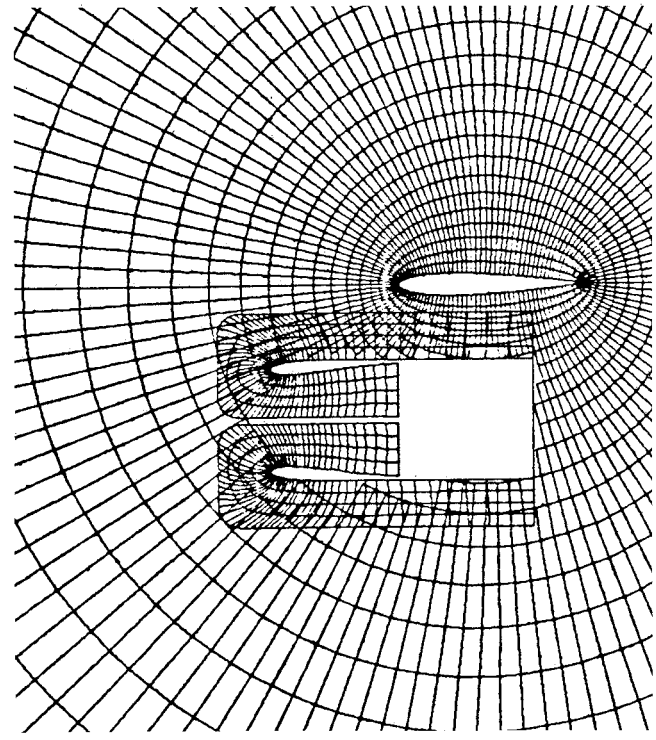

Fig. 6 Side view of NACA 0012-wing/GELAC1-nacelle configuration global grid.

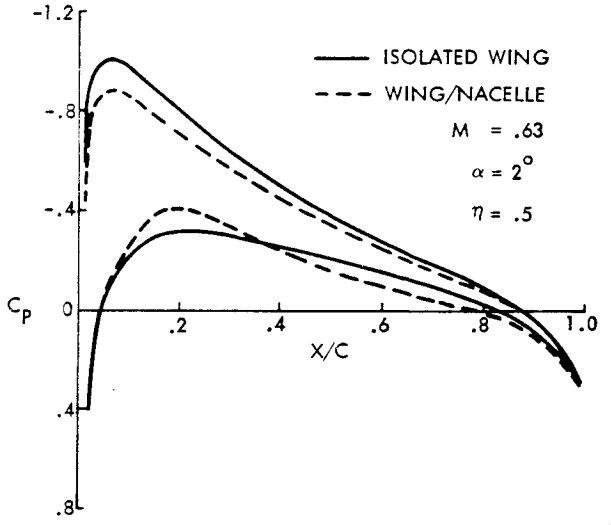


Fig. 7 Wing pressure distribution for NACA 0012-wing/GELAC1-nacelle configuration at $M_\infty = 0.63$ and $\alpha = 2$ deg.

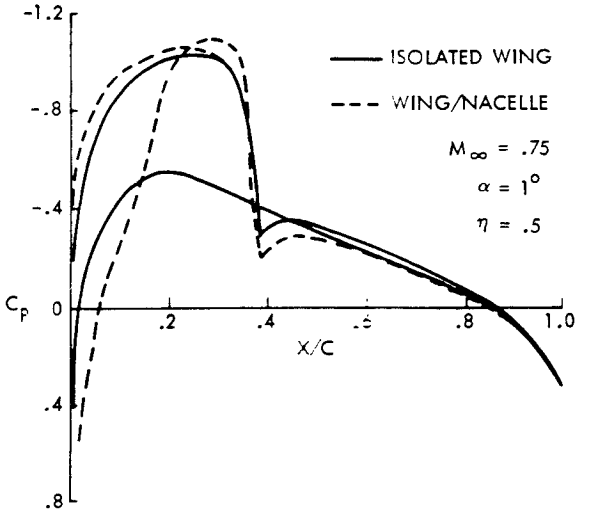


Fig. 8 Wing pressure distribution for NACA 0012-wing/GELAC1-nacelle configuration at $M_\infty = 0.75$ and $\alpha = 1$ deg.

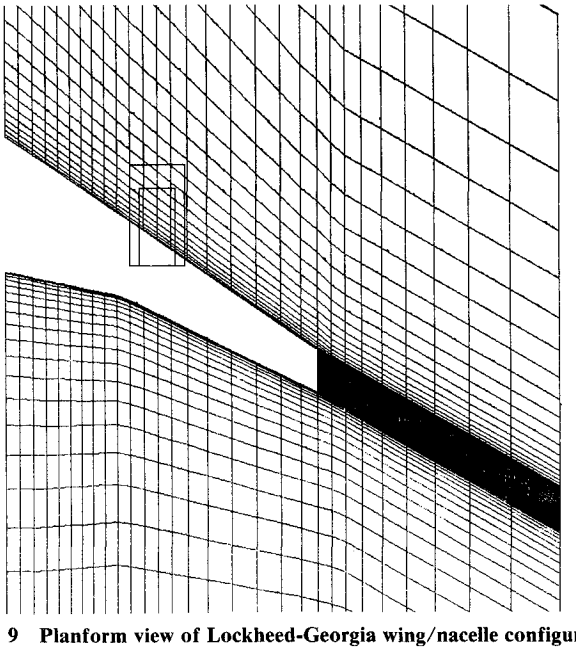

Fig. 9 Planform view of Lockheed-Georgia wing/nacelle configuration global grid.

The grid topologies used for this wing/nacelle multicomponent configuration are illustrated in Figs. 4-6. Figure 5 shows a frontal view of the composite-overlapped grid system. A side view of the composite grid system at the span station coincident with the nacelle-symmetry plane is given in Fig. 6. The overlap region between the wing O-grid and the nacelle C-grid is clearly illustrated in this figure. The nacelle interface grid is illustrated in isolation in Fig. 4. The wing component grid for this case consisted of 101 wraparound stations, 22 spanwise stations, and 30 normal stations. The nacelle component grid consisted of 67 wraparound stations, 13 circumferential stations, and 5 radial stations.

Figure 7 illustrates the computed surface solution for this wing/nacelle configuration at a freestream Mach number $M_\infty$ of 0.63 at an angle of attack $\alpha$ of 2.0 deg. Shown in this figure is the surface pressure coefficient $C_P$ vs the fractional distance along the chord $X/C$ (distance/chord length) for the 50% span station ($\eta = 0.5$). Results are presented for the wing/nacelle multicomponent flow calculation and for an isolated-wing calculation. The wing/nacelle calculation was performed assuming that the inlet capture ratio was 0.7 and the ratio of the engine exhaust-plane velocity to the freestream velocity was 2.25. A three-point extrapolation formula was used to establish the potential values at the back end of the nacelle from the prescribed jet-exhaust velocity ratio. The effect of including the nacelle is to reduce the suction level on the upper wing surface and to increase it on the lower surface near the aft portion of the nacelle (wing leading edge). The high engine-exhaust jet velocity increases the flow velocity near the lower wing surface, thereby reducing the circulation and hence the lift. The midspan wing-section lift coefficient for the isolated wing calculation was 0.287. For the wing/nacelle calculation, the midspan section-lift coefficient was reduced to 0.24. These results agree qualitatively with what is observed experimentally.[11] The wing/nacelle mutual-interference calculation required four cycles through both the wing and nacelle component algorithms to achieve convergence, which corresponds to a three-order-of-magnitude reduction in the maximum residual. The computation required approximately 5 h of CPU execution time on the DEC VAX-11/780 computer. Approximately one-million words of core storage were required for the computation.

Figure 8 illustrates the computed midspan-wing-pressure distribution for the NACA 0012-wing/GELAC1-inlet configuration for the conditions of a freestream Mach number of 0.75 and 1-deg angle of attack. For this computation, the inlet capture ratio was maintained at 0.7 but the ratio of the engine exit-plane velocity to the freestream velocity was now equated to 1.15. In this case, the wing upper-surface pressure distribution is slightly altered by the presence of the nacelle; however, the lower-surface pressure distribution is markedly different. In this case, the lower-surface flow undergoes a rapid expansion followed by a strong shock at the 40% chord location. The net effect is a reduction in the sectional lift. These results indicate that the sense and magnitude of the nacelle-interference effects are strongly dependent on the exhaust-jet velocity, freestream conditions, and nacelle location.

The next set of computed results is for a recently designed Lockheed-Georgia wing/nacelle configuration. The wing geometry employs supercritical airfoil sections and is both swept and tapered. The nacelle geometry is again the GELAC1 axisymmetric-nacelle/inlet configuration. The nacelle plane of symmetry is again located at the wing midspan ($\eta = 0.5$). Figure 9 illustrates a planform view of the wing and nacelle. The wing component grid employed 101 wraparound stations, 22 spanwise stations, and 30 normal stations. The nacelle component grid employed 67 wraparound stations, 13 circumferential stations, and 5 radial stations.

Figures 10 and 11 present the computed wing pressure distributions for this wing/nacelle configuration at the 46 and 60% span stations, respectively. The freestream Mach number and incidence used in the computations correspond to 0.77

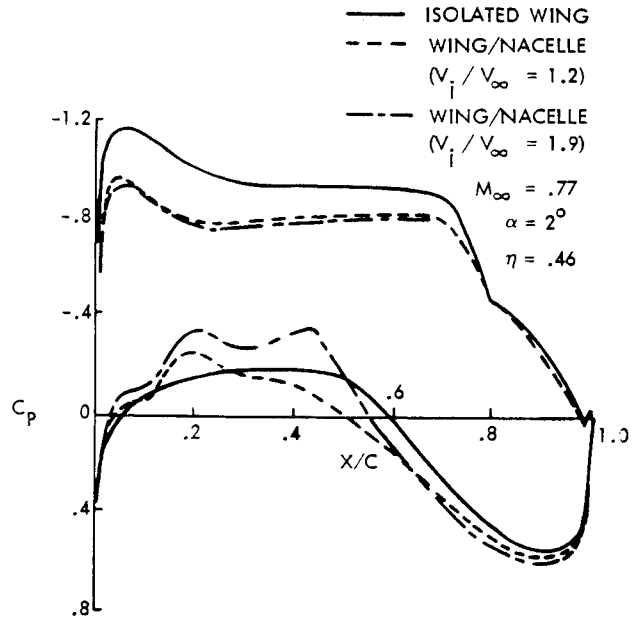


**Fig. 10 Wing pressure distribution for Lockheed-Georgia wing/nacelle configuration at 46% span.**

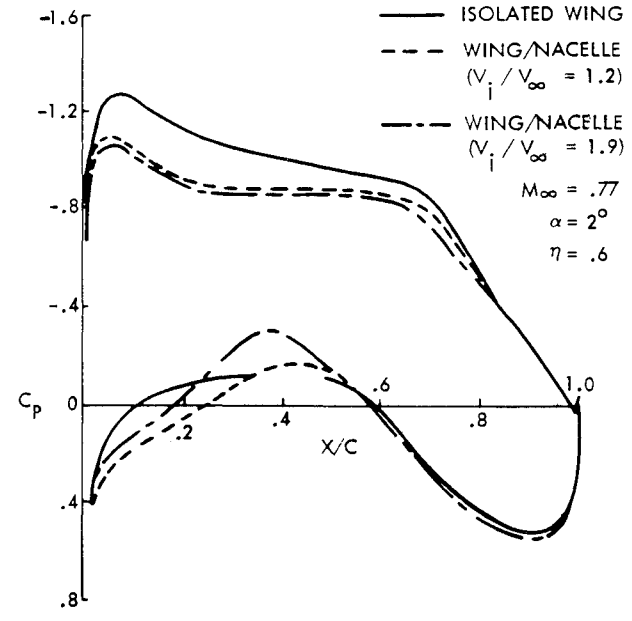


**Fig. 11 Wing pressure distribution for Lockheed-Georgia wing/nacelle configuration at 60% span.**

and 2 deg, respectively. On each of the two figures, the computed solution is shown for an isolated-wing calculation and for wing/nacelle calculations using exhaust-jet/freestream-velocity ratios ($v_i/v_\infty$) of 1.2 and 1.9. The inlet capture ratio was 0.7. The nacelle interference effect for each of the two spanwise locations was to reduce the suction level on the wing upper surface with this effect being more pronounced as the exhaust-jet velocity was increased. As the upper-surface suction level was reduced, the shock was moved slightly forward for each of the two span locations. The interference effect of the nacelle on the wing lower surface was to increase the suction levels near midchord. Again this effect was more pronounced at the higher exhaust-jet velocity. On the lower surface near the wing leading edge, the surface pressure was higher for the wing/nacelle configuration than for the isolated wing, except at the inboard station where the pressures were comparable. For all of the span stations illustrated, the interference effect of the nacelle decreased the section-lift coefficients as compared to the isolated wing results. Moreover, the reduction in sectional lift became more pronounced as the exhaust-jet velocity was increased. Overall, the computed effects of the nacelle interference with the wing flowfield agree qualitatively with experimental observations.

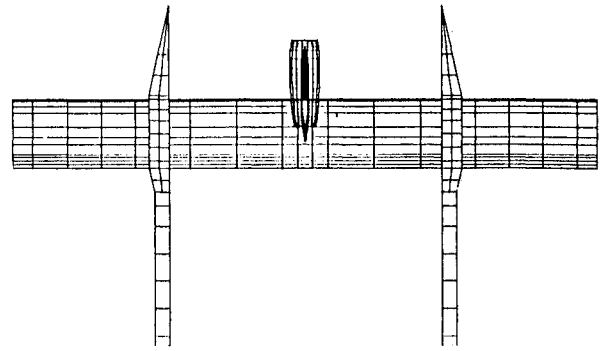

**Fig. 12 Planform view of NASA Langley wing/pylon/nacelle configuration.**

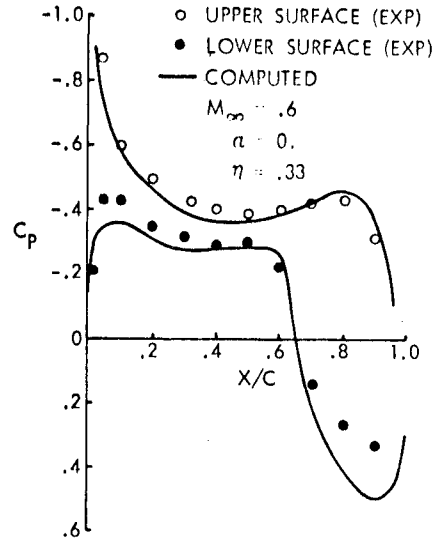


**Fig. 13 Wing pressure distribution for NASA Langley isolated wing at $\eta = 0.3375$.**

The final set of results presents correlations of numerical solutions with experimental data for an isolated wing and a wing/pylon/nacelle configuration tested by Carlson and Compton.[12] This configuration consisted of an unswept, untapered, and untwisted supercritical wing, a swept and tapered pylon, and an axisymmetric flow-through nacelle. The wing was attached to a bifurcated support strut system. A top view of the test configuration and support system is given in Fig. 12. Blunt and sharp interchangeable leading edges for the wing, pylon, and nacelle were employed in the experimental investigation. The numerical results presented herein correspond to the test configuration with the blunt leading edges. Correlation studies were performed for the case of a freestream Mach number $M_\infty$ of 0.6 and zero incidence ($\alpha = 0$ deg).

Carlson and Compton[12] measured surface pressures for both an isolated wing and a wing/pylon/nacelle configuration. Shown in Figs. 13 and 14 are comparisons of the computed pressure distributions and experimental data for two spanwise locations on the isolated wing configuration. Here, the nondimensional spanwise coordinate is defined as $\eta = y/y_T$, where $y$ is the spanwise distance measured from the span station of the nacelle centerline, and $y_t$ the spanwise

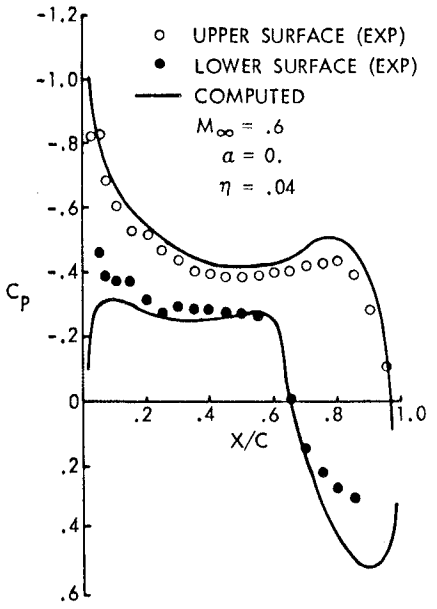


Fig. 14 Wing pressure distribution for NASA Langley isolated wing at $\eta = 0.043$.

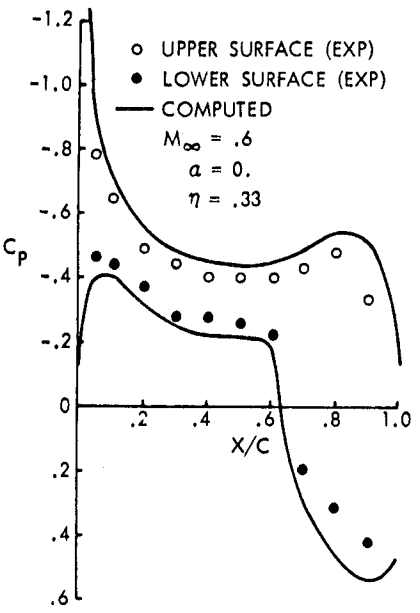


Fig. 16 Wing pressure distribution for NASA Langley wing/pylon/nacelle configuration at $\eta = 0.3375$.

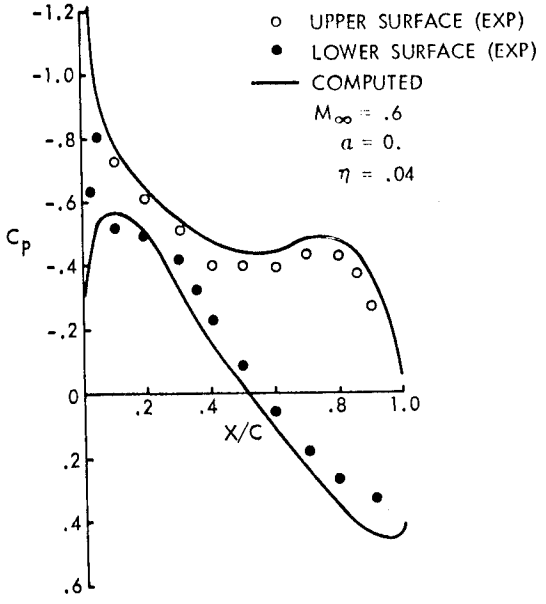


Fig. 15 Wing pressure distribution for NASA Langley wing/pylon/nacelle configuration at $\eta = 0.043$.

distance between the nacelle centerline span station and the support strut (see Fig. 12). The results presented in Figs. 13 and 14 correspond to $\eta = 0.043$ and 0.3375. Generally, good agreement is obtained at these two span stations. The differences between theory and experiment near the trailing edge on the wing lower surface are attributable mainly to the neglect of viscous effects in the numerical model. A computational grid using 120 wraparound stations, 26 span stations, and 25 radial stations was employed in obtaining the solution.

Correlations of the computed and measured wing pressure distributions for the wing/pylon/nacelle multicomponent configuration are illustrated in Figs. 15 and 16, which correspond to spanwise locations of $\eta = 0.043$ and 0.3375, respectively. It should be noted that the pylon and strut were not modeled in the numerical analysis. Nonetheless, generally good agreement is obtained between theory and experiment. Compared to the isolated wing results, inclusion of the nacelle (and pylon) creates a lower-surface suction peak at approximately the 10% chordwise location. The lower-surface pressure distribution is markedly altered from the plateau-type distribution when the propulsion system installation effects are included in the computation. This behavior is mitigated as the distance from the nacelle span station is increased, as is noted by comparing Fig. 16 with Fig. 15. The multicomponent flowfield solution was obtained using the same wing grid as in the isolated wing case, and by using a nacelle grid with 67 wraparound stations, 13 circumferential stations, and 5 radial stations. To simulate the conditions of a flow-through nacelle, an effective compressor face Mach number of 0.5 and an exhaust-jet/freestream velocity ratio of 0.9 were used in the computation.

## Conclusions

An efficient grid interfacing zonal algorithm has been developed to compute the three-dimensional transonic flowfield about wing-nacelle multicomponent configurations. In the present approach, a component-adaptive grid-embedding scheme has been employed in which the global computational grid is composed of a series of overlapped component grids, where each component grid is optimized for a particular geometry, such as the wing or nacelle. The AF2 approximate factorization algorithm is used to determine the full-potential equation solution on each component grid with trivariate interpolation being used to transfer property information between the grids. The optimized grid system produces the desired balance between convergence speed and accuracy of the flowfield solution.

## Acknowledgments

This effort was sponsored in part by the NASA Ames Research Center under Contract NAS2-11285 and in part by the Lockheed Independent Research and Development Program.

## References

[1]Boppe, C. W. and Aidala, P. V., "Complex Configuration Analysis at Transonic Speeds," AGARD CP 285, 1980.

[2]Yu, N. J., "Grid Generation and Transonic Flow Calculations for Three Dimensional Configurations," AIAA Paper 80-1391, 1980.

[3]Atta, E. H. and Vadyak, J., "A Grid Embedding Transonic Flow Analysis Computer Program for Wing/Nacelle Configurations," NASA CR-166529, 1983.

[4]Ballhaus, W. F., Jameson, A., and Albert, J., "Implicit Approximate-Factorization Schemes for Steady Transonic Flow Problems," *AIAA Journal,* Vol. 16, June 1978, pp. 573-579.

[5]Holst, T. L., "An Implicit Algorithm for the Conservative Transonic Full Potential Equation Using an Arbitrary Mesh," *AIAA Journal,* Vol. 17, Oct. 1979, pp. 1038-1045.

[6]Holst, T. L. and Thomas, S. D., "Numerical Solution of Transonic Wing Flow Fields," AIAA Paper 82-0105, Jan. 1982.

[7]Vadyak, J. and Atta, E. H., "A Computer Program for the Calculation of Three-Dimensional Transonic Nacelle/Inlet Flowfields," NASA CR-166528, 1983.

[8]Atta, E. H. and Vadyak, J., "A Grid Overlapping Scheme for Flowfield Computations About Multicomponent Configurations," *AIAA Journal,* Vol. 21, Sept. 1983, pp. 1271-1277.

[9]Sorensen, R. L., "A Computer Program to Generate Two-Dimensional Grids About Airfoils and Other Shapes by Use of Poisson's Equation," NASA TM-81198, 1980.

[10]Atta, E. H., "Component-Adaptive Grid Interfacing," AIAA Paper 81-0382, Jan. 1981.

[11]Harris, A. E. and Pauley, G. I., "Simulation Techniques for Pylon-Mounted Turbo-Fan Engines," Aircraft Research Association Ltd., Bedford, England, Report 36, Oct. 1975.

[12]Carlson, J. R. and Compton, W. B., "An Experimental Investigation of Nacelle-Pylon Installation on an Unswept Wing at Subsonic and Transonic Speeds," NASA TP 2246, 1984.